BROOKHAVEN
NATIONAL LABORATORY

BNL-113638-2017-JA

Flexible Heteroepitaxy of $CoFe_2O_4$/Muscovite Bimorph with Large Magnetostriction

Heng-Jui Liu, Chih-Kuo Wang, Dong Su , Tahta Amrillah, Ying-Hui Hsieh, Kun-Hong Wu, Yi-Chun Chen, Jenh-Yih Juang, Lukas M. Eng, Shien-Uang Jen, and Ying-Hao Chu

Submitted to ACS Appl. Mater. Interfaces

January 2017

Center for Functional Nanomaterials

Brookhaven National Laboratory

U.S. Department of Energy
USDOE Office of Science (SC),
Basic Energy Sciences (SC-22)

Notice: This manuscript has been authored by employees of Brookhaven Science Associates, LLC under Contract No. DE- SC0012704 with the U.S. Department of Energy. The publisher by accepting the manuscript for publication acknowledges that the United States Government retains a non-exclusive, paid-up, irrevocable, world-wide license to publish or reproduce the published form of this manuscript, or allow others to do so, for United States Government purposes.

DISCLAIMER

This report was prepared as an account of work sponsored by an agency of the United States Government. Neither the United States Government nor any agency thereof, nor any of their employees, nor any of their contractors, subcontractors, or their employees, makes any warranty, express or implied, or assumes any legal liability or responsibility for the accuracy, completeness, or any third party's use or the results of such use of any information, apparatus, product, or process disclosed, or represents that its use would not infringe privately owned rights. Reference herein to any specific commercial product, process, or service by trade name, trademark, manufacturer, or otherwise, does not necessarily constitute or imply its endorsement, recommendation, or favoring by the United States Government or any agency thereof or its contractors or subcontractors. The views and opinions of authors expressed herein do not necessarily state or reflect those of the United States Government or any agency thereof.

Heteroepitaxial $CoFe_2O_4$/Muscovite Bimorph with Large Magnetostriction for Flexible Electronics

Chih-Kuo Wang[1], Heng-Jui Liu[1], Dong Su[2], Tahta Amrillah[3], Ying-Hui Hsieh[1,4], Kun-Hong Wu[5], Yi-Chun Chen[5], Jenh-Yih Juang[3], Lukas M. Eng[4], Shien-Uang Jen[6,7*], and Ying-Hao Chu[1,3,6*]

[1]*Department of Materials Science and Engineering, National Chiao Tung University, Hsinchu 30010, Taiwan*

[2]*Center for Functional Nanomaterials, Brookhaven National Laboratory, NY 11973, United States*

[3]*Department of Electrophysics, National Chiao Tung University, Hsinchu 30010, Taiwan*

[4]*Institut fur Angewandte Photophysik, Technische Universitat Dresden, Dresden 01069, Germany*

[5]*Department of Physics, National Cheng Kung University, Tainan 701, Taiwan*

[6]*Institute of Physics, Academia Sinica, Taipei 11529, Taiwan*

[7]*Institute of Optoelectronic Science, National Taiwan Ocean University, Keelung 20224, Taiwan*

*physjen@gate.sinica.edu.tw *and yhc@nctu.edu.tw*

Over the past decades, a quick rise of flexible devices revolutionizes electronics into a new era of applications, such as rollable displays (*1-3*), bendable solar cells (*4*), wearable electronics (*5*), biotechnologies (*6, 7*), etc. They gradually change personal habits in our daily life. In order to expand practical applications of flexible electronics, the integration of more functional materials on flexible substrates are highly on demand, especially the one with its properties coupled to a deformation. For example, magnetostriction is a phenomenon that represents the relationship between the degree of deformation (or strain state) and the magnetic state of a ferromagnet, which can be quantified by a physical parameter called "magnetostrictive coefficient" (λ). Namely, the dimension of a ferromagnet can be varied when a magnetic field is applied, or the magnetic anisotropy can be modulated by deforming the ferromagnet. Various applications such as magnetic MEMs and magnetoelectric sensors are all built based on this principle. Thus, the integration of magnetostrictive materials offers a good opportunity of adding magnetic feature to expand the functionalities of flexible

electronics. In addition, in the path of achieving the miniaturization of devices, a bimorph (film and substrate) form becomes inevitable. Conceptually, a bimorph combining flexible substrates could exhibit more competitive advantages than the traditional one using rigid substrates for magnetostrictive devices. For instances, the dimensional change of bimorph would acquire a higher response to magnetic field and the flexible devices are more convenient to carry and can fit any shape of object for operation.

In order to make flexible magnetostrictive devices with the best performance, the epitaxial growth of thin film is crucial since the magnetostriciton of magnetic materials is strongly correlated with crystal orientation. In this study, spinel $CoFe_2O_4$ (CFO) is adopted as a model system because it possesses superior magnetic properties with high Curie temperature (793K) (*8*), large magnetocrystalline and magnetostrictive anisotropy (*9-12*). To achieve the integration of epitaxial CFO film on a flexible substrate, the strong connection between CFO films and flexible substrates are highly desired. To make these new coming technologies practical, substrates with specific requirements such as pliancy, durability, thermal stability, and compatibility of present fabrication processes are always the prime considerations. Observing the commercially available flexible substrates, most of them are made of polymer and amorphous materials. However, none of them can really satisfy all requirements so far. In the pursuit of proper flexible substrates for the integration of future electronics, muscovite sheets, a group of layered materials, has attracted attention increasingly due to its great potential to overcome the technical difficulties found in polymer substrates. For example, muscovite (or we can simplify it as "Mica") is flexible and transparent when the thickness is below 100 um and the melting point (with the range of 1150 K to 1300 K) is high (*13*) to be used in modern thin film process. Moreover, compared to polymer substrates, Mica has a well ordered crystal structure, on which many popular inorganic materials such as metal dichalcogenides or oxides can be grown epitaxially (*14-17*). These successful examples inspire us to attempt the fabrication of epitaxial CFO films on Mica that could trigger more possibilities of developing novel multifunctional electronics driven by magnetostriction (*18*).

The samples were prepared by using pulsed laser deposition (PLD). The growth process was *in situ* monitored by reflective high energy electron diffraction (RHEED) (Fig. 1A). Before the deposition, a clean and flat surface of Mica substrate was prepared through a standard procedure: First, Mica sheets are taped on the smooth and flat surface of a metal brick. Because Mica can be viewed as the assemblage of numerous layered sheets that are piled up through van der Waals force. Hence, we can use a sharp tweezer to cleave Mica easily. Finally, a very clean and atomic flat (001)

surface can be obtained in the cleaved side of the separated Mica. The RHEED patterns of air-cleaved bare Mica substrate recorded with the electron beam along [100] and [010] directions show the 2D Laue diffraction dots accompanying with sharp streaks. Such a characteristic confirms that the surface of Mica is extremely flat and could be adopted for sequential deposition of the CFO film. When the deposition started, the RHEED patterns of Mica substrate quickly disappeared in a short time. Instead, a new streaky pattern of CFO emerged as shown in Fig. 1B. Interestingly, while we traced the variation of the intensity around the central diffraction spots in RHEED, it showed regular oscillations, suggesting a layer-by-layer growth mode of CFO on Mica substrate (Fig. 1C). Based on the atomic force microscopic (AFM) images (Fig. 1D), we found the topography of both Mica substrate and CFO thin film show a very smooth surface with the root-mean-square roughness (R_{rms}) of 0.18 nm and 0.55 nm, respectively. Based on the distance between streaks in the RHEED patterns, the in-plane epitaxial relation of the CFO film and Mica substrate can be identified as CFO[$1\,\bar{1}\,0$]||Mica[010] and CFO[$\bar{1}\bar{1}\,2$]||Mica[100]. Therefore, the out-of-plane epitaxy of CFO[111]||Mica[001] can also be determined. Moreover, the atomic structures of surface and simulated reciprocal lattices along Mica [001] and CFO [111] zone axes are compared as shown in Fig. 1D. Generally, monoclinic Mica simultaneously possesses a pseudo-hexagonal lattice on its layered plane (*14, 15*). It leads to a repetition of the RHEED patterns of Mica either along [010] or [100] every 60^o intervals in the azimuth rotation (left panel in Fig. 1E). The (111) oriented CFO film also exhibits the resembling phenomena in the RHEED patterns of CFO[$1\bar{1}0$] and CFO[$11\bar{2}$]. It can be easily realized from the simulated in-plane reciprocal lattice with the zone axis of CFO [111], where both {$2\bar{2}0$} and {$22\bar{4}$} of CFO naturally present six variants (right panel in Fig. 1E). Such an in-plane structural similarity between Mica and CFO provide a good opportunity for the development of high quality heteroepitaxy.

The detailed crystal structure of CFO/Mica bimorph was then investigated by a combination of x-ray diffraction (XRD), Raman spectra, and transmission electron microscopy (TEM). First, the out-of-plane (OOP) XRD shows only the diffraction peaks of Mica (00L) and CFO (HHH) reflections (Fig. 2A), suggesting that highly crystalline CFO film was grown without any other orientations or secondary phases. A magnified section of the XRD curve around $Mica(004)_m$ shown in the inset of Fig. 2A displays clear thickness fringes, indicating sharp interface and smooth surface. The estimation of film thickness is ~50 nm based on the spacing of thickness fringes. According to the peak positions of the CFO film in the x-ray normal scan and the reciprocal space map (Fig. 2B), the d-spacings of CFO (111) and ($3\bar{1}\bar{1}$) are calculated as 4.910Å and 2.555 Å. Compared to the respective bulk d-spacings of 4.846 Å and

2.531 Å, the CFO film shows an increase in both OOP (+1.3%) and IP (+0.95%) lattice parameters, which is probably due to the cation redistribution in the spinel structure or the oxygen vacancies induced in the environment of low oxygen pressure during the deposition. The ϕ-scans of CFO (004) and Mica (202) reflections were also conducted to confirm the IP structural relation, as shown in Fig. 2C. The intensity of three peaks is not equivalent (one is very strong and the other two are very weak) in the azimuth scan of Mica (202) suggesting a nearly perfect single-domain feature because Mica (202) plane originally presents no symmetry due to its monoclinic tilting angle between *a*- and *c*- axis (β=100°). On the other hand, the azimuthal scan of CFO (004) shows a three-fold symmetry, consistent with the typical single-domain feature with the rotation pole along [111] in cubic CFO. The well alignment of Mica (202) and CFO (004) peaks at 0°, 120°, and 240° azimuthal angles suggests the in-plane epitaxial relationship as CFO[$11\bar{2}$]||Mica[100], which agrees with the results of RHEED excellently.

The symmetry of the CFO film on Mica was investigated by Raman spectroscopy. A standard CFO film grown on (111) oriented STO substrate was adopted as a reference sample. As shown in Fig. 2D, the Raman spectra of both CFO films grown on Mica and STO (111) show six phonon modes. In general, ideal CFO is an inverse spinel with the space group of $Fd\bar{3}m$, which possesses five active Raman modes: 693 cm^{-1} (A_{1g}), 566 cm^{-1} (T_{2g}), 471 cm^{-1} (T_{2g}), 309 cm^{-1} (E_g), and 183 cm^{-1} (T_{2g}). However, this ideal inverse spinel structure is usually not stable under the influence of strain and defects. Such a result easily causes the cation redistribution in the tetrahedral (T_d) and octahedral sites (O_h) (*19-21*) or a short-range ordering of cation (*22*), leading to an additional A_{1g} phonon mode observed at ~626 cm^{-1}. Moreover, the intensity variation and the frequency shift of phonon modes of the films on both substrates indicate a slight distortion of CFO crystal structure.

In order to further investigate the interface of CFO/mica bimorph, high-resolution transmission electron microscopy (HR-TEM) was employed. A cross-sectional HR-TEM image unveils a superior heteroepitaxy of highly crystalline CFO film without detectable defects and grain boundaries on Mica as shown in Fig. 2E. A negligible variation of the contrast in the HR-TEM image implies a nearly uniform strain state of the CFO film. Two insets of the electron diffraction patterns from the selected areas of the CFO film and Mica substrate are clearly indexed in Fig. 2E, confirming the epitaxial relation observed in the results of RHEED and XRD. The interface between CFO and Mica displays an ultra-thin interdiffused layer within 1nm (<1 u.c. c-axis of Mica). Such an interdiffusion could cause a stronger atomic bonding between CFO and Mica, and then behave as a seeding layer for further coherent growth. This speculation is supported by the intensity profile of RHEED, where

several irregular oscillations are typically observed in the initial stage that implies a dramatic change of the surface structure.

After the establishment on the structural feature of CFO/Mica bimorph, the attention is paid to its functionalities. Through applying superconducting quantum interference device (SQUID) magnetometer, the magnetic hysteresis loops along the OOP and IP directions (Fig. 3A) were obtained to reveal the magnetic properties and the corresponding magnetic anisotropy of CFO/Mica bimorph. Both loops show a typical ferromagnetic characteristic with a saturation magnetization (M_S) of ~150 emu/cm^3. Noting that no significant magnetic anisotropy is observed in the either OOP or IP hysteresis loop, implying a small strain in the CFO film. According to the ref. (*23*), the effective anisotropy constants along the OOP and IP directions ($K_{eff, OOP}$ and $K_{eff, IP}$) estimated form the loops are ~ 4.31×10^{-6} erg/cm^3 and 4.44×10^{-6} erg/cm^3, respectively. Besides, it is also known that the CFO single crystal possesses a large magnetocrystalline anisotropy constant (K_1~2×10^6 erg/cm^3) (*24*), and therefore the effective anisotropy constants of the respective projections along [111] (OOP) and [$1\bar{1}0$] (IP) can be obtained as ~1.15×10^{-6} erg/cm^3 and 1.414×10^{-6} erg/cm^3. The enhancement of anisotropy constants experimentally compared to the theoretical estimation can be ascribed to the slightly distorted CFO lattice observed in the Raman measurement. However, both results show a small difference between $K_{eff, OOP}$ and $K_{eff, IP}$, suggesting that the magnetocrystalline anisotropy should still dominate the magnetic behavior of the CFO film. Moreover, the variation of CFO magnetic anisotropy under various bending states has also been revealed in Fig. 3B. In each bending case, the radius of curvature of the CFO film was controlled approximate 1.77 mm. Interestingly, the IP magnetic hysteresis loops measured at the unbending condition and the inward bending conditions along both long edge and short edge, have exhibited no significant difference. It implies that this flexible CFO/Mica bimorph shows solid magnetic performance no matter how it is bent. Such a result can be strongly supported by the micromagnetic behaviors of the CFO film obtained from magnetic force microscopy (MFM). Figs. 3 C-F illustrate the evolution of magnetic domains in the CFO film during the bending process. Before the measurement, the CFO film was magnetized at 5 Tesla along IP direction (along long edge). In the free-state case (Fig. 3C), only one edge of the CFO film was fixed. Its MFM image presents that a ratio of two opposite OOP components is nearly equal to one (the red and blue contrasts are around 51.5% and 48.5%, respectively). This implies that the CFO film prefers to stay in its demagnetization state. According to the magnetic hysteresis loops from both IP and OOP directions, a very small magnetic anisotropy in the CFO/Mica bimorph was found, which is consistent with these randomly distributed upward and downward magnetic domains observed in the MFM image.

Afterwards, the CFO/Mica bimorph was bended up to 26 μm and then down to 8 μm (Fig. 3D-F). The red circles marked in these MFM images are used to indicate the same region of the measurement for all bending conditions. Here it clearly shows that the distribution of the magnetic domains in the CFO film still remains as the free-state case, which can perfectly support the results of magnetic hysteresis measurements. Based on these results, the robust magnetic properties of the CFO/Mica bimorph is revealed, deliver a new pathway to flexible electronics with magnetic feature.

The controllable deformation by a magnetic field is the most important feature of magnetostrictive effect. The digital holographic microscope (DHM) was adopted to measure the magnetostrictive performance of the CFO/Mica bimorph (*25*). This technique allows us to quantify the magnetostriction coefficient of the CFO film on Mica by mapping out the altitude of the CFO/Mica bimorph under external either longitudinal magnetic field ($H_{\parallel}$) along the length (L) (parallel to CFO $[1\bar{1}0]$) or transvers field ($H_{\perp}$) along the width (W) (parallel to CFO $[\bar{1}\bar{1}2]$), as the schematics shown in Fig. 4A. The deflection profile shows that the bimorph bends up 473 nm under the longitudinal magnetic field of 2000 Oe, whereas it bends down about 172 nm under the same transverse field. The longitudinal and transverse magnetostritcion coefficients ($\lambda_{\parallel}$ and $\lambda_{\perp}$ respectively) can be given by (*26*):

$$\lambda_{\mathrm{P}} = -\left(\frac{1}{3}\right)\left[\frac{\Delta z_{\mathrm{P}}}{L^2}\right]K$$

$$\lambda_{\perp} = -\left(\frac{1}{3}\right)\left[\frac{\Delta z_{\perp}}{L^2}\right]K$$

$$K \equiv \left(\frac{E_s}{E_f}\right)\left(\frac{t_s^2}{t_f}\right)\left[\left(\frac{1+\nu_f}{1+\nu_s}\right)\right] \qquad (1)$$

where the *s* and *f* subscripts stand for the substrate and film respectively, *E* is the Young's modulus, *t* means the thickness factor, and *v* is the Poisson's ratio. The sample size for the measurement is 6 mm by 2 mm with the thickness of the film and the substrate being approximately 100 nm and 60 μm, respectively. The Young's moduli of muscovite and CFO are 60 GPa (*27*) and 141.6 GPa (*28*), respectively. The values of Poisson's ratio of are 0.25 (*29*) and 0.26 (*30*) respectively for muscovite and CFO. Therefore, the difference of magnetostrction coefficient ($\Delta\lambda$) of the CFO film can be derived by the following equation,

$$\Delta\lambda = (\lambda_{\mathrm{P}} - \lambda_{\perp}) \qquad (2)$$

Fig. 4B is the variation of $\Delta\lambda$ verse the sample length. It has been found that $\Delta\lambda$ would be overestimated due to the length factor (L) in the denominator of the

equation (1) when the measurement moves toward the fixed end (L=0 mm). Hence, a fitting curve in the flatter region (L > 3mm) is performed and extrapolated to L=0 mm for obtaining more accurate $\Delta\lambda$ of the CFO film, which is ~-104 ppm. In comparison with the experimental result, we also use the following equation to derive the magnetostrictive coefficient of CFO single crystal along its $[1\bar{1}0]$ and $[\bar{1}\bar{1}2]$ direction (*31*):

$$\lambda = \frac{2}{3}\lambda_{100}\left(\alpha_1^2\beta_1^2 + \alpha_2^2\beta_2^2 + \alpha_3^2\beta_3^2 - \frac{1}{3}\right) + 3\lambda_{111}\left(\alpha_1\alpha_2\beta_1\beta_2 + \alpha_2\alpha_3\beta_2\beta_3 + \alpha_1\alpha_3\beta_1\beta_3\right) \quad (3)$$

where the magnetostrictive coefficient λ_{100} is -590×10^{-6} and λ_{111} is 120×10^{-6} (*9*), and the α_i and β_i are the magnetization and cosine angle of the strain measurement respectively to the cubic axis. The calculated value of $\lambda_{1\bar{1}0}$ of ideal single crystal form is -57.2×10^{-6}, which is in good agreement with the experimental value ($\lambda_{\parallel}$) of -64×10^{-6}. However, the calculated value of $\lambda_{\bar{1}\bar{1}2}$ is 117.5×10^{-6}, significantly different from the experimental value ($\lambda_{\perp}$) of 40×10^{-6}. Therefore, $\Delta\lambda$ of the CFO film is smaller than that of the ideal CFO single crystal (-175 ppm). Such a discrepancy between experimental value and theoretical value can be attributed to two reasons. First, recalling that the sample is fabricated as a cantilever form so that the preference of magnetization is along the longitudinal edge of sample ($[1\bar{1}0]$ direction of this CFO film) due to the shape induced demagnetization state. Additionally, because of the limitation of the instrument setup, the maximum magnetic field can only reach 2 kOe during the measurement, which is far from the saturation magnetic field (~30 kOe). It leads to an underestimation of $\Delta\lambda$ in the CFO film. Based on these results, the superior magnetostrictive properties of the CFO/Mica bimorph are delivered for practical applications.

To sum up, we have fabricated a new magnetostrictive bimorph composed by a heteroepitaxy of the CFO film and a flexible Mica. This system shows a layer-by-layer growth mode, indicating a strong bonding between the film and substrate. Such a compact connection provides a wonderful platform for the operation of the magnetostrictive material. The robust magnetic properties as well as the controllable deformation of the CFO/Mica heterostructure utilizing the magnetic force have been demonstrated. This study highlights the great potential of flexible magnetostrictive films for future soft technologies.

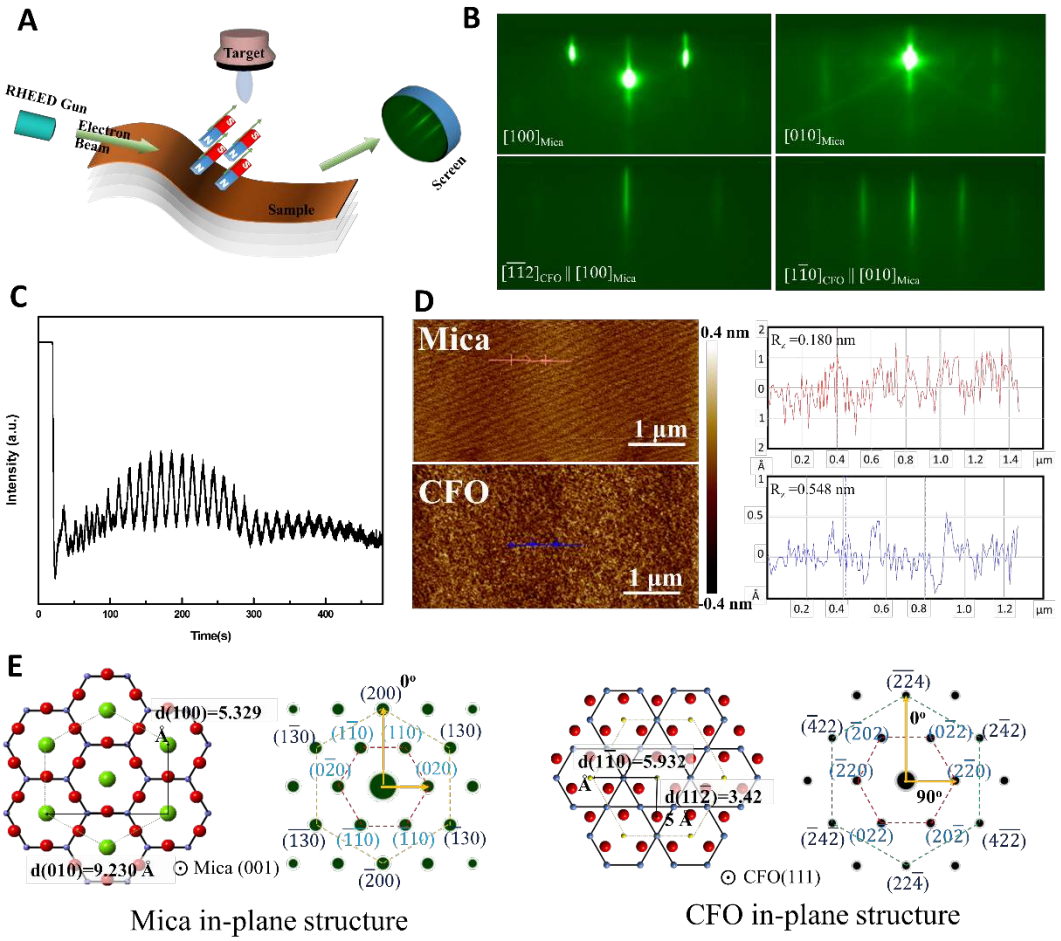

Fig. 1. (A) Schematic of deposition process for flexible magnetic film monitored by RHEED in real time. (B) Two top panels are typical RHEED patterns of pure Mica (before deposition) along its [100] and [010] directions, whereas the other two bottom panels are patterns of the CFO film (after deposition) along its $[11\bar{2}]$ and $[1\bar{1}0]$ directions. (C) The intensity profile of RHEED during deposition of CFO presents clear oscillations, indicating the film follows the layer-by-layer growth mode. (D) AFM topography images of both the Mica substrate and the CFO film show a very smooth surface, where the corresponding root-mean-square roughness is ~0.18nm for Mica and ~0.548nm for the CFO thin film. (E) The surface structures of both Mica and CFO show a quasi-hexagonal lattice, leading to the presence of six-fold symmetry in their corresponding reciprocal spaces.

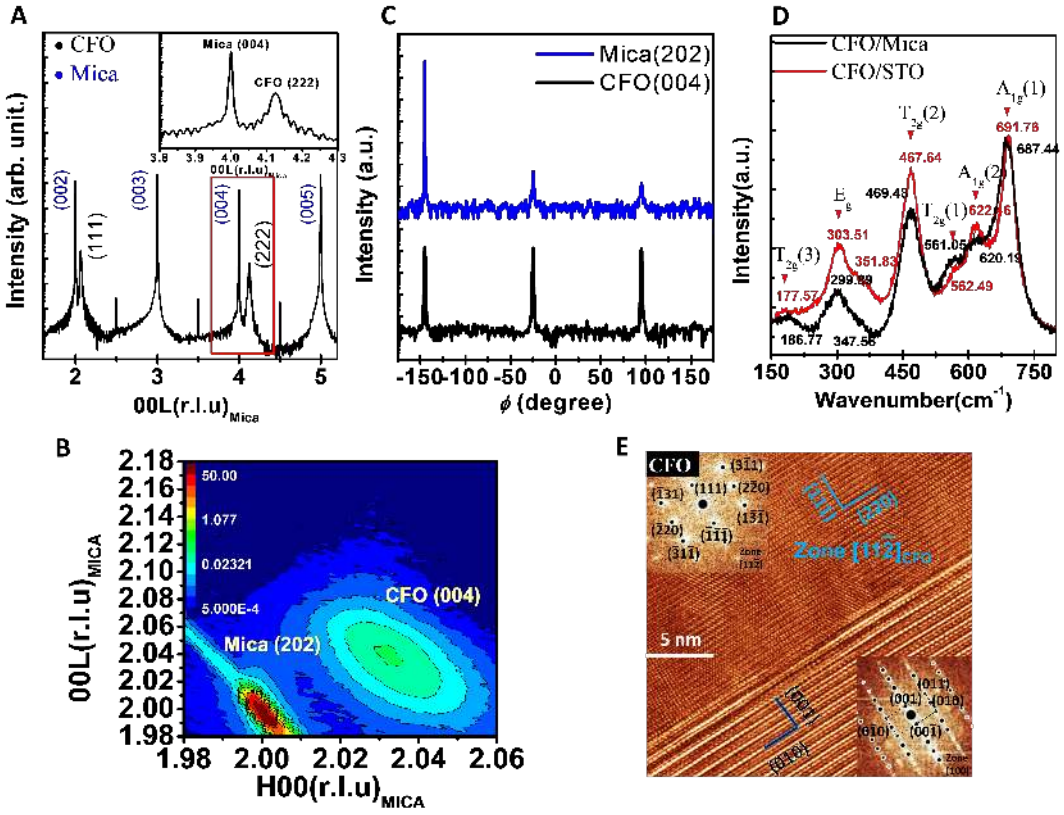

Fig. 2. (A) X-ray normal scan shows only the (00l) series peaks of Mica and (111) series peaks of CFO. Inset is the magnified region around the Mica (004) and CFO (222) peaks, where clear thickness fringes can be observed. (B) Asymmetry reciprocal space map around Mica (202) peak along with CFO (004) peak. (C) ϕ scans of Mica (202) and CFO (004). (D) Raman spectra of the CFO thin films on Mica and STO. (E) The cross-sectional high-resolution TEM image shows the CFO thin film grown on the Mica substrate. Insets are the corresponding electron diffraction patterns, illustrating the in-plane heteroepitaxy between CFO and Mica.

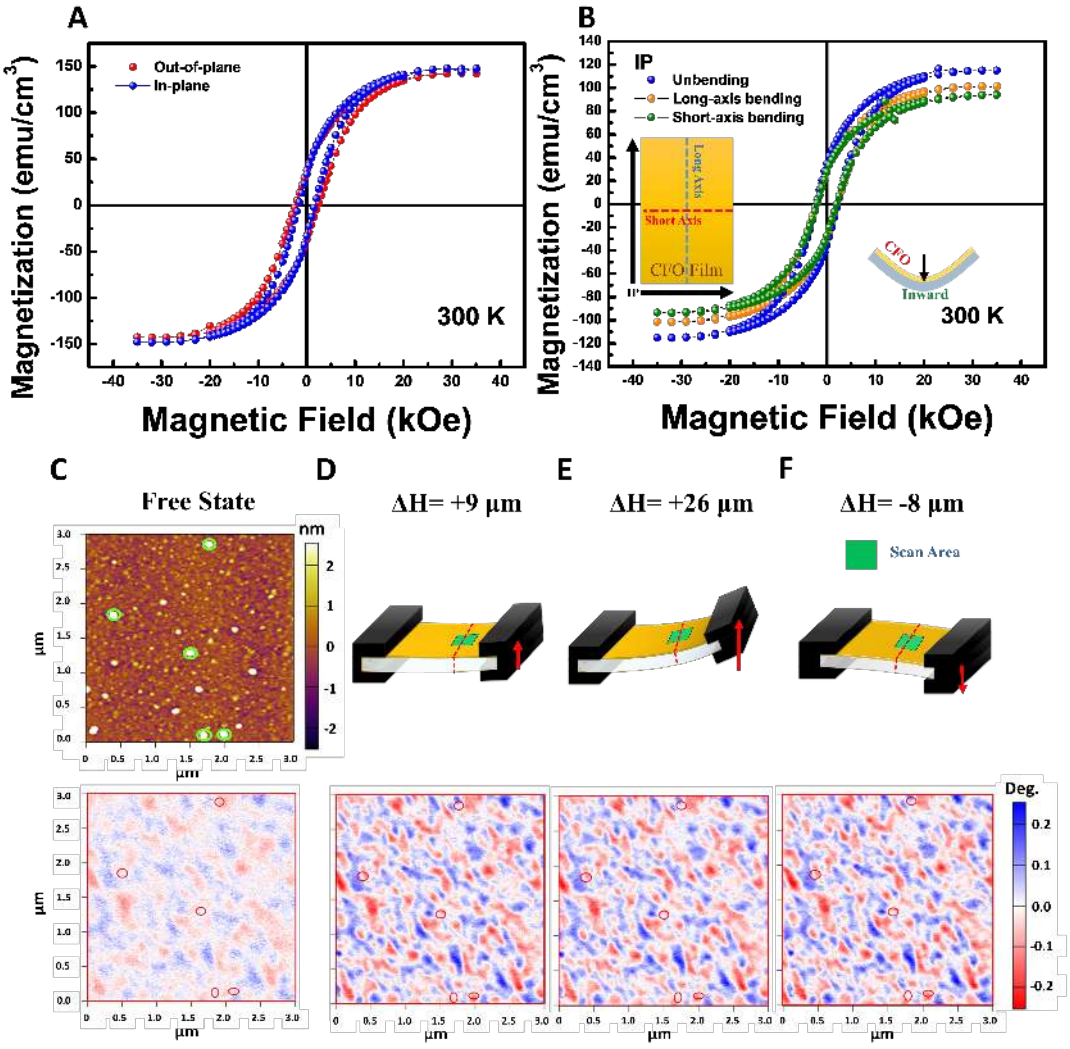

Fig. 3. (A) The hysteresis loops measured by applying the magnetic field along out-of-plane (red) and in-plane (blue) directions. (B) The magnetic hysteresis loops measured with long-axis (orange), short-axis (olive) and without (blue) the bending state. (C) The upper panel is the morphology of the CFO film from AFM image, and lower panel is the corresponding MFM image. The upper panels are the schematics of the bending CFO film (D) upward to 9 μm, (E) 26 μm, and then (F) downward to 8 μm, and the lower panels are the corresponding MFM of each bending state.

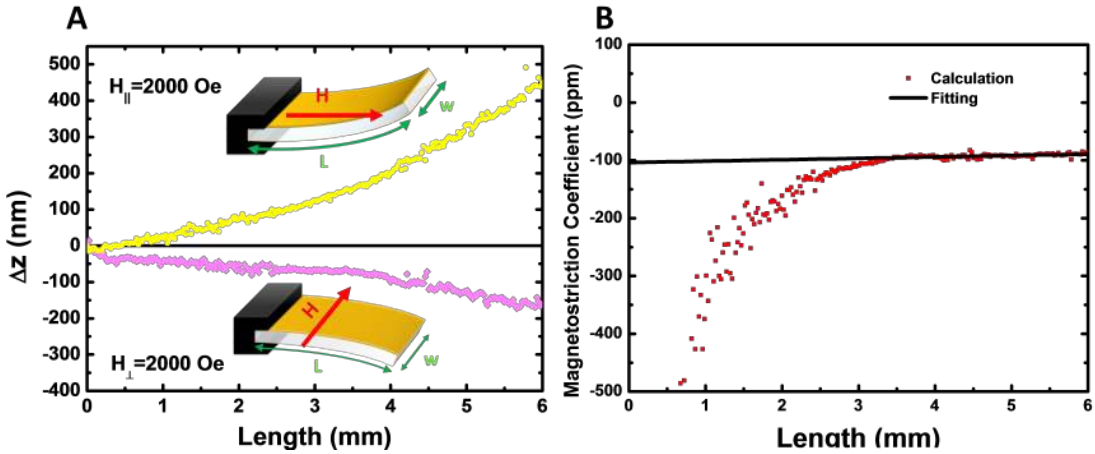

Fig. 4. (A) The deflection profiles of bimorph under external fields of longitudinal magnetic field ($H_{\parallel}$) and transvers field ($H_{\perp}$). (B) The saturated magnetostriction coefficient verse the sample length are extracted from Fig. 4A according to Eq. (2).

Primary Sources

Secondary Sources

Uncategorized References

1. D. Tobjörk, R. Österbacka, Paper Electronics. *Advanced Materials* **23**, 1935-1961 (2011)10.1002/adma.201004692).
2. Y. Fujisaki, H. Koga, Y. Nakajima, M. Nakata, H. Tsuji, T. Yamamoto, T. Kurita, M. Nogi, N. Shimidzu, Flexible Electronics: Transparent Nanopaper-Based Flexible Organic Thin-Film Transistor Array (Adv. Funct. Mater. 12/2014). *Advanced Functional Materials* **24**, 1656-1656 (2014)10.1002/adfm.201470077).
3. L. Zhou, A. Wanga, S.-C. Wu, J. Sun, S. Park, T. N. Jackson, All-organic active matrix flexible display. *Applied Physics Letters* **88**, 083502 (2006)doi:http://dx.doi.org/10.1063/1.2178213).
4. J. Yoon, A. J. Baca, S.-I. Park, P. Elvikis, J. B. Geddes, L. Li, R. H. Kim, J. Xiao, S. Wang, T.-H. Kim, M. J. Motala, B. Y. Ahn, E. B. Duoss, J. A. Lewis, R. G. Nuzzo, P. M. Ferreira, Y. Huang, A. Rockett, J. A. Rogers, Ultrathin silicon solar microcells for semitransparent, mechanically flexible and microconcentrator module designs. *Nat Mater* **7**, 907-915 (2008); published online Epub11//print (http://www.nature.com/nmat/journal/v7/n11/suppinfo/nmat2287_S1.html).
5. W. Zeng, L. Shu, Q. Li, S. Chen, F. Wang, X.-M. Tao, Fiber-Based Wearable Electronics: A Review of Materials, Fabrication, Devices, and Applications. *Advanced Materials* **26**, 5310-5336 (2014)10.1002/adma.201400633).
6. S. C. B. Mannsfeld, B. C. K. Tee, R. M. Stoltenberg, C. V. H. H. Chen, S. Barman, B. V. O. Muir, A. N. Sokolov, C. Reese, Z. Bao, Highly sensitive flexible pressure sensors with microstructured rubber dielectric layers. *Nat Mater* **9**, 859-864 (2010); published online Epub10//print (http://www.nature.com/nmat/journal/v9/n10/abs/nmat2834.html#supplementary-information).
7. D.-H. Kim, N. Lu, R. Ma, Y.-S. Kim, R.-H. Kim, S. Wang, J. Wu, S. M. Won, H. Tao, A. Islam, K. J. Yu, T.-i. Kim, R. Chowdhury, M. Ying, L. Xu, M. Li, H.-J. Chung, H. Keum, M. McCormick, P. Liu, Y.-W. Zhang, F. G. Omenetto, Y. Huang, T. Coleman, J. A. Rogers, Epidermal Electronics. *Science* **333**, 838-843 (2011); published online EpubAugust 12, 2011 (10.1126/science.1206157).
8. L. Bouet, P. Tailhades, A. Rousset, Relations between magneto-optical properties and reactivity in cobalt-manganese ferrite thin films and powders.

Journal of Magnetism and Magnetic Materials **153**, 389-396 (1996); published online Epub2/2/ (http://dx.doi.org/10.1016/0304-8853(95)00564-1).

9. R. M. Bozorth, E. F. Tilden, A. J. Williams, Anisotropy and Magnetostriction of Some Ferrites. *Physical Review* **99**, 1788-1798 (1955); published online Epub09/15/ (
10. J. C. Slonczewski, Origin of Magnetic Anisotropy in Cobalt-Substituted Magnetite. *Physical Review* **110**, 1341-1348 (1958); published online Epub06/15/ (
11. Y. X. Zheng, Q. Q. Cao, C. L. Zhang, H. C. Xuan, L. Y. Wang, D. H. Wang, Y. W. Du, Study of uniaxial magnetism and enhanced magnetostriction in magnetic-annealed polycrystalline $CoFe_2O_4$. *Journal of Applied Physics* **110**, 043908 (2011)doi:http://dx.doi.org/10.1063/1.3624661).
12. D. Fritsch, C. Ederer, Epitaxial strain effects in the spinel ferrites $CoFe_2O_4$ and $NiFe_2O_4$ from first principles. *Physical Review B* **82**, 104117 (2010); published online Epub09/23/ (
13. S. G. Barlow, D. A. C. Manning, Influence of time and temperature on reactions and transformations of muscovite mica. *British Ceramic Transactions* **98**, 122-126 (1999)doi:10.1179/096797899680327).
14. K. Saiki, K. Ueno, T. Shimada, A. Koma, Application of Van der Waals epitaxy to highly heterogeneous systems. *Journal of Crystal Growth* **95**, 603-606 (1989); published online Epub1989/02/02 (http://dx.doi.org/10.1016/0022-0248(89)90475-2).
15. K. Ueno, K. Saiki, T. Shimada, A. Koma, Epitaxial growth of transition metal dichalcogenides on cleaved faces of mica. *Journal of Vacuum Science & Technology A* **8**, 68-72 (1990)doi:http://dx.doi.org/10.1116/1.576983).
16. K. Wang, Y. Liu, W. Wang, N. Meyer, L. H. Bao, L. He, M. R. Lang, Z. G. Chen, X. Y. Che, K. Post, J. Zou, D. N. Basov, K. L. Wang, F. Xiu, High-quality Bi2Te3 thin films grown on mica substrates for potential optoelectronic applications. *Applied Physics Letters* **103**, 031605 (2013)doi:http://dx.doi.org/10.1063/1.4813903).
17. S. Steinberg, W. Ducker, G. Vigil, C. Hyukjin, C. Frank, M. Z. Tseng, D. R. Clarke, J. N. Israelachvili, Van der Waals Epitaxial Growth of α-Alumina Nanocrystals on Mica. *Science* **260**, 656-659 (1993); published online EpubApril 30, 1993 (10.1126/science.260.5108.656).
18. P. Yu, Y.-H. Chu, R. Ramesh, Oxide interfaces: pathways to novel phenomena. *Materials Today* **15**, 320-327 (2012); published online Epub7// (http://dx.doi.org/10.1016/S1369-7021(12)70137-2).

19. P. Chandramohan, M. P. Srinivasan, S. Velmurugan, S. V. Narasimhan, Cation distribution and particle size effect on Raman spectrum of CoFe2O4. *Journal of Solid State Chemistry* **184**, 89-96 (2011); published online Epub1// (http://dx.doi.org/10.1016/j.jssc.2010.10.019).
20. Y. Y. Liao, Y. W. Li, Z. G. Hu, J. H. Chu, Temperature dependent phonon Raman scattering of highly a-axis oriented $CoFe_2O_4$ inverse spinel ferromagnetic films grown by pulsed laser deposition. *Applied Physics Letters* **100**, 071905 (2012)doi:http://dx.doi.org/10.1063/1.3683520).
21. H.-J. Liu, Y.-Y. Liu, C.-Y. Tsai, S.-C. Liao, Y.-J. Chen, H.-J. Lin, C.-H. Lai, W.-F. Hsieh, J.-Y. Li, C.-T. Chen, Q. He, Y.-H. Chu, Tuning the functionalities of a mesocrystal via structural coupling. *Scientific Reports* **5**, 12073 (2015); published online Epub07/14/online (10.1038/srep12073).
22. V. G. Ivanov, M. V. Abrashev, M. N. Iliev, M. M. Gospodinov, J. Meen, M. I. Aroyo, Short-range B-site ordering in the inverse spinel ferrite $NiFe_2O_4$. *Physical Review B* **82**, 024104 (2010); published online Epub07/15/ (
23. T. Dhakal, D. Mukherjee, R. Hyde, P. Mukherjee, M. H. Phan, H. Srikanth, S. Witanachchi, Magnetic anisotropy and field switching in cobalt ferrite thin films deposited by pulsed laser ablation. *Journal of Applied Physics* **107**, 053914 (2010)doi:http://dx.doi.org/10.1063/1.3327424).
24. M. Khodaei, S. A. Seyyed Ebrahimi, Y. Park, J. Ok, J. Kim, J. Son, S. Baik, Enhancement of in-plane magnetic anisotropy in (111)-oriented Co0.8Fe2.2O4 thin film by deposition of PZT top layer. *Appl. Phys. A* **117**, 1153-1160 (2014); published online Epub2014/11/01 (10.1007/s00339-014-8486-0).
25. J. Shien-Uang, L. Chi-Ching, C. Shin-Ting, Magnetostriction Measurement of a Ferromagnetic Thin Film Using Digital Holographic Microscope. *Magnetics, IEEE Transactions on* **50**, 1-4 (2014)10.1109/TMAG.2014.2324633).
26. E. du Trémolet de Lacheisserie, J. C. Peuzin, Magnetostriction and internal stresses in thin films: the cantilever method revisited. *Journal of Magnetism and Magnetic Materials* **136**, 189-196 (1994); published online Epub1994/09/01 (http://dx.doi.org/10.1016/0304-8853(94)90464-2).
27. L. E. McNeil, M. Grimsditch, Elastic moduli of muscovite mica. *Journal of Physics: Condensed Matter* **5**, 1681 (1993).
28. H. Zheng, J. Wang, S. E. Lofland, Z. Ma, L. Mohaddes-Ardabili, T. Zhao, L. Salamanca-Riba, S. R. Shinde, S. B. Ogale, F. Bai, D. Viehland, Y. Jia, D. G. Schlom, M. Wuttig, A. Roytburd, R. Ramesh, Multiferroic BaTiO3-CoFe2O4 Nanostructures. *Science* **303**, 661-663 (2004); published online EpubJanuary 30, 2004 (10.1126/science.1094207).

29. A. Castellanos-Gomez, M. Poot, A. Amor-Amorós, G. A. Steele, H. S. J. Zant, N. Agraït, G. Rubio-Bollinger, Mechanical properties of freely suspended atomically thin dielectric layers of mica. *Nano Research* **5**, 550-557 (2012)10.1007/s12274-012-0240-3).
30. S. R. Murthy, ΔE-effect in Co□Zn ferrites. *Crystal Research and Technology* **25**, 461-466 (1990)10.1002/crat.2170250420).
31. C. D. G. B. D. Cullity, in *Introduction to magnetic materials*. (IEEE, Hoboken, 2009), chap. 8, pp. 243-246.